S, N-doped carbon dots-based cisplatin delivery system in adenocarcinoma cells: Spectroscopical and computational approach

Tanja Dučić [a,*], Carla S. Alves [b], Željko Vučinić [c], Juan M. Lázaro-Martínez [d], Marijana Petković [e], Juan Soto [f], Dragosav Mutavdžić [c], M. Valle Martínez de Yuso [g], Ksenija Radotić [c,*], Manuel Algarra [h,*]

[a] ALBA-CELLS Synchrotron, MIRAS Beamline, Cerdanyola del Vallès, Barcelona. Spain
[b] CQM- Madeira Chemistry Research Centre, University of Madeira, Funchal, Portugal
[c] Institute for Multidisciplinary Research, University of Belgrade, Belgrade, Serbia
[d] Department of Chemistry and IQUIMEFA-UBA-CONICET, Facultad de Farmacia y Bioquímica, Universidad de Buenos Aires, Ciudad Autónoma de Buenos Aires, Argentina
[e] Center for light-based research and technologies COHERENCE, Department of Atomic Physics, Vinča Institute of Nuclear Sciences, National Institute of the Republic of Serbia, University of Belgrade, Belgrade, Serbia
[f] Dept. Physical Chemistry. Faculty of Science, University of Málaga, 29071 Málaga, Spain
[g] Central Service to Support Research Building (SCAI). The University of Málaga. Málaga, Spain
[h] INAMAT² - Institute for Advanced Materials and Mathematics. Department of Science. Public University of Navarra. Campus de Arrosadia, 31006 Pamplona, Spain

GRAPHICAL ABSTRACT
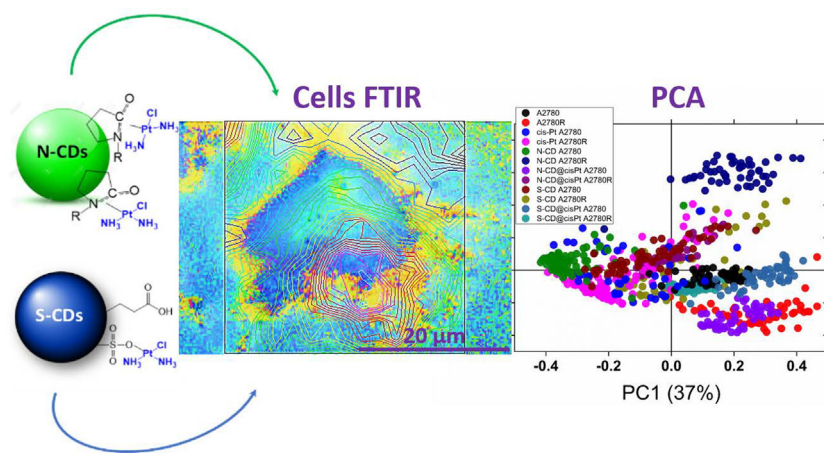
ARTICLE INFO

ABSTRACT

S and N-doped carbon dots (S-CDs and N-CDs) and their cisplatin (cis-Pt) derivatives.

(S-CDs@cis-Pt and N-CDs@cis-Pt) were tested on two ovarian cancer cell lines: A2780 and A2780 cells resistant to cis-Pt (A2780R). Several spectroscopic techniques were employed to check S-CDs@cis-Pt and N-CDs@cis-Pt: solid- and solution-state nuclear magnetic resonance, matrix-assisted laser desorption, ionization time-of-flight mass spectrometry, and X-ray photoelectron spectroscopy. In addition, synchrotron-based Fourier Transformed Infrared spectro-microscopy was used to evaluate the biochemical changes in cells after treatment with cis-Pt, S-CDs, N-CDs, or S-CDs@cis-Pt and N-CDs@cis-Pt, respectively. Computational chemistry was applied to establish the model for the most stable bond between S-CDs and N-CDs and cis-Pt. The results revealed the successful modification of S-CDs and N-CDs with cis-Pt and the formation of a stable composite system that can be used for drug delivery to cancer cells

* Corresponding authors.
  E-mail addresses: tducic@cells.es (T. Dučić), manuel.algarra@unavarra.es (M. Algarra).

and likewise to overcome acquired cis-Pt resistance. Nanoparticle treatment of A2780 and A2780R cells led to the changes in their structure of lipids, proteins, and nucleic acids depending on the treatment. The results showed the S-CDs@*cis*-Pt and *N*-CDs@*cis*-Pt might be used in the combination with *cis*-Pt to treat the adenocarcinoma, thus having a potential to be further developed as drug delivery systems.

1. Introduction

Epithelial ovarian cancer (EOC) is one of the most lethal gynecological malignancies in Western society [1,2]. Characterized by at least five distinct histological subtypes [1], this highly heterogeneous disease is primarily associated with poor survival prognosis [3]. Therefore, patients undergo cytoreductive surgery for epithelial ovarian carcinomas (EOC) treatment followed by combination chemotherapy using *Pt*-based compounds and Taxol® [1,2]. This approach is practical as the first line of treatment for many ovarian cancer patients.

However, up to 75% of patients are reported to relapse, eventually developing resistance to chemotherapy, and finally succumbing to the disease [4]. Various treatment strategies and new cytotoxic agents such as doxorubicin, 5-fluorouracil, paclitaxel, or docetaxel have been developed and tested over the years to overcome the cisplatin (*cis*-Pt) resistance. Even so, patient survival rates have remained relatively unchanged [1,2]. *Cis*-Pt is a well-known, effective, broad-spectrum anticancer drug used in therapy over several decades [4–9]. However, it forms crosslinks with the purine bases of DNA, which interferes with the DNA repair mechanisms, leading to DNA damage and subsequent cancer cell death [4]. As a result, many patients eventually develop *cis*-Pt resistance along with severe side-effects, such as nephropathy or ototoxicity [4,5]. These side-effects contributed to a marked reduction in *cis*-Pt's clinical applications and are thus one of the significant challenges in ovarian cancer therapy and a limiting factor in patient survival [1–5]. The effectiveness of *cis*-Pt as a chemotherapeutic agent lies in its capacity to enter cells via different routes [4–9]. Also, it has multiple cell targets, which allow for the formation of many different DNA-Pt adducts [4,5]. However, these combined processes initiate a self-defense mechanism in human cells where various genes are activated or silenced, resulting in dramatic epigenetic and/or genetic alternations [5]. This cascade of events leads to the development of *cis*-Pt resistance.

There is an urgent need to develop a novel therapeutic approach to overcome *cis*-Pt resistance in EOC patients. One of the promising approaches is the coupling of *cis*-Pt with a carrier, such as nanoparticles. Carbon dots (CDs) have become an attractive group of NPs used in several fields, including nanomedicine and bio-imaging [10], because of their high chemical stability, dispersibility in water, low photo-bleaching, and high biocompatibility [11]. Thus, they are ideal candidates for drug delivery along with cellular imaging in the physiological environment [12,13]. Previous studies have demonstrated that the cellular uptake of CDs in cancer cell lines was generally efficient resulting in the labeling of the cells with bright fluorescence emissions from predominantly cell membrane and cytoplasm [14]. In our previous investigation, we synthesized organic CDs for potential bio-imaging applications and characterized them using various spectroscopic methods [15]. The results obtained with preosteoblasts mouse cells incubated with CDs demonstrated a precise cellular contour without any functionalization of CDs [12,16].

In the present work, we characterized S-CDs and *N*-CDs and their respectively functionalized with *cis*-Pt (S-CDs@*cis*-Pt and *N*-CDs@*cis*-Pt) and test them as a novel agent for adenocarcinoma treatment, on two EOC cell types. These cell types are

well-characterized ovarian cancer cell lines, one being sensitive to cisplatin (*i.e.* the A2780), and the second is *cis*-Pt resistant (*i.e.* the A2780R). To characterize the intracellular changes triggered with these S-CDs and *N*-CDs and S-CDs@*cis*-Pt and *N*-CDs@*cis*-Pt, we applied the synchrotron-based Fourier Transformed Infrared (SR-FTIR) micro-spectroscopy and X-ray photoelectron spectroscopy (XPS). The presence of the S-CDs@*cis*-Pt and *N*-CDs@*cis*-Pt in the different cell lines enables efficient, bright fluorescence emissions predominantly from cell membrane and cytoplasm and the evaluation of the role of the CDs in the delivery of cisplatin intracellularly. Techniques applied also allowed to check the differences in the localization of accumulated S-CDs and *N*-CDs, S-CDs@*cis*-Pt and *N*-CDs@*cis*-Pt depending on the cell line's resistance towards *cis*-Pt. The position, presence and relative intensity of bands related to the proteins', phospholipids' and nucleic acids' functional groups were the base for estimation of changes in biologically relevant macromolecules, and thus intracellular structures in the cytoplasm, membranes, and nucleus, respectively, induced by the treatments with S-CDs and *N*-CDs, *cis*-Pt and their derivates S-CDs@*cis*-Pt and *N*-CDs@*cis*-Pt respectively.

2. Experimental

2.1. Synthesis of cisplatin derivates (S and N-CDs@cis-Pt)

The structures and synthetic routes for the preparation of the two CDs linked to *cis*-diammineplatinum(II) dichloride (99.9 %, Sigma-Aldrich, Germany) are labelled through the text as S and *N*-CDs@*cis*-Pt. The preparation of the S and *N*-CDs, was described in the previous publication [16], in which poly(sodium-4-styrene sulfonate) and polyvinylpyrrolidone (PVP) were used as S and N sources respectively. The synthesis of S-CDs@*cis*-Pt was performed by dissolving *cis*-Pt (152.1 mg / 0.5 mmol; 8.3 mM) in H_2O (60 mL), followed by the addition of S-CDs solution in H_2O (20 mg/mL). For the preparation of *N*-CDs@*cis*-Pt, *cis*-Pt (67.5 mg / 0.23 mmol, 8.51 mM) was dissolved in H_2O (27 mL) by the addition of 2 mL of *N*-CDs (17.75 mg/mL) in ultra-pure water. Both solutions were left stirred overnight.

2.2. Physicochemical characterization

2.2.1. NMR Experiments.

Solid-(*ss*-NMR) and solution-state Nuclear Magnetic Resonance (*ls*-NMR) experimental data were acquired with a Bruker Avance-III HD spectrometer (Bremen, Germany) equipped with a 14.1 T narrow bore magnet operating at Larmor frequencies of 600.09 MHz and 150.91 MHz for ^{1}H and ^{13}C, respectively. Powdered samples were packed into 3.2 or 2.5 mm ZrO_2 rotors and rotated at room temperature at magic angle spinning (MAS) rates of 15 or 35 kHz, respectively. ^{13}C-CP-MAS (cross-polarization and magic angle spinning) experiments were done in a 3.2 mm MAS probe. Glycine was used as an external reference compound to record the ^{13}C spectra and to set the Hartmann-Hahn matching condition in the CP-MAS experiments in ^{13}C spectra. The contact time during CP was 2000 μs. The SPINAL64 sequence (small phase incremental alternation with 64 steps) was used for heteronuclear decoupling during acquisition [17]. ^{1}H-MAS *ss*-NMR spectra were

recorded in a 2.5 mm MAS probe using single pulse excitation experiments. Chemical shifts for ^{1}H (in ppm) are relative to $(CH_3)_4Si$.

2.2.2. X-ray photoelectron spectroscopy (XPS).

XPS measurements were carried out on a Physical Electronics PHI VersaProbe II spectrometer (Feldkirchen, Germany) using monochromatic Al-K$_\alpha$ radiation (49.1 W, 15 kV and 1486.6 eV). C 1 s, O 1 s and N 1 s core-level spectra were analyzed. Spectra were recorded with a constant pass energy value of 29.35 eV, using a 100 μm diameter circular analysis area, and analyzed using PHI SmartSoft software and processed using MultiPak 9.3 package. Shirley-type background and Gauss-Lorentz curves were used to determine the binding energies. The binding energy values were referenced to the adventitious carbon C 1 s signal (284.8 eV).

2.2.3. Synchrotron-based Fourier transform infrared (FTIR) micro-spectroscopy

The FTIR measurements were carried out at the MIRAS station at the synchrotron ALBA (Barcelona, Spain). Recently, we showed that this method is very effective to study intact cancer cells after different treatments without any staining and chemical or mechanical changes [18]. The infrared (IR) spectra were collected in a transmission mode using an infrared microscope coupled to an FTIR Hyperion 3000 spectrometer (Bruker, Germany) and a liquid nitrogen-cooled mercury cadmium telluride (MCT) detector. The aperture slits were set to 10×10 μm to achieve the single-cell size, and each spectrum was acquired after 256 scans at 4 cm^{-1} spectral resolution. The FTIR transmission mode was used to collect spectra of single cells ranging from 900 to 3100 cm^{-1}. The FTIR spectra were acquired from N = 55–100 individual A2780 and A2780R ovarian cancer cells grown on the 10×0.5 mm CaF$_2$ window and treated with different CDs (where control was not submitted to any treatment) and afterward fixed with 4% formaldehyde prior to analysis.

2.2.4. Pre-processing of spectral data

Baseline correction of the raw spectra and the multiplicative scatter correction were used as pretreatment to reduce the additive and multiplicative effects in the spectra. Then, all single spectra were vector normalised, and they were further subjected to the Principal component analysis (PCA). PCA is a statistical procedure that allows orthogonal transformation, mostly of highly correlated variables, such as those found in FTIR spectra, into a set of uncorrelated data called principal components. These components are arranged so that the first principal component has the most significant variance; the second is uncorrelated with the first. Finally, it absorbs the maximum of the remaining variance. Mathematically, PCA can be represented by the following model: $\mathbf{X} = \mathbf{TP}^T + \mathbf{E}$, where is $\mathbf{T}$ score matrix, $\mathbf{P}$ loading matrix and $\mathbf{E}$ is the residual matrix, so it is $\mathbf{P}^T\mathbf{P} = \mathbf{I}$ ($\mathbf{I}$ is the identity matrix). The spectral pre-processing was performed in the OPUS software, while the Unscrambler and Quasar softwares were was used for PCA.

2.2.5. MALDI TOF/TOF mass spectrometry

Matrix-assisted time of flight mass spectrometry (MALDI TOF/TOF MS Bruker Autoflex MaX, Bremen, Germany) was used to determine the binding of *cis*-Pt to S and *N*-CDs respectively. S-CDs and *N*-CDs were suspended in water at a concentration of approximately 1 mg/mL. For some measurements, solution of S-CDs and *N*-CDs was mixed with organic matrix before application on MALDI target. The spectra were also acquired in a matrix-free LDI mode (1 μL of solution per spot). Samples were afterwards left at room temperature to crystallize. As matrices, either 2,5-dihydroxybenzoic acid (DHB) or α-cyano-hydroxycinnamic acid (CHCA) (10 mgmL^{-1} in 50% methanol) were used. MALDI mass spectra were acquired in the positive ion mode in the reflector mode and 170 ns delay time. Accelerating voltage was set to 20 kV, laser repetition rate 200 Hz, and laser fluency kept around 10% over the threshold to acquire the optimum signal-to-noise ratio. Each spectrum represents the average of 2000 individual laser shots.

2.2.6. Cell preparation

The ovarian cancer cells (A2780) and *cis*-Pt-resistant ovarian cancer cells (A2780R) were grown in RPMI 1640 medium supplemented with 10% (v/v) fetal bovine serum, 1% (v/v) antibiotic–antimycotic solution, L-glutamine (2 mM), and 1% (w/v) of cisplatin (100 mM). In the case of the A2780R cells, *cis*-Pt was only used in the subculturing process prior to performing the MTT assay. The cells were harvested, cultured (10 000 cells/well) and incubated with cisplatin, S-CDs, *N*-CDs, or S and *N*-CDs@*cis*-Pt in a concentration range of 0–10 μM (concentration of *cis*-Pt in formulations was S-CDs@*cis*-Pt and *N*-CDs@*cis*-Pt) for 48 h. Metabolic activity was determined by the MTT assay, according to the procedure described earlier [19]. Briefly, the evaluation of cell viability with the MTT assay commenced by replacing the culture medium with a fresh culture medium containing 10% (v/v) of an MTT solution (0.5 mg/mL). A 3-h-incubation followed this in the dark to achieve the formation of the formazan crystals. After the incubation, generated formazan crystals were dissolved in dimethyl sulfoxide (DMSO), and the absorbance was measured at 550 nm. The mean value of the blank was subtracted from each sample. Samples were incubated in a quadruplicate, and the mean values were calculated. Values obtained for non-treated cells were set to 100%, and other values were expressed as % of control values.

2.2.7. Computational

The interactions of cisplatin with *N*-CDs and S-CDs have been studied using density functional theory (DFT) with the hybrid exchange–correlation functional CAM-B3LYP [20]. The def2-TZV basis sets have been applied to all the atoms which form the systems under study [21,22]. The electronic structure calculations were carried out with GAUSSIAN16 [23]. Adsorption energies were determined using the expressions given by Thermodynamics Statistical with programs implemented by our research group [24,25]. The potential energy surfaces that lead to the formation of the complexes formed between cisplatin and (S-CDs and *N*-CDs) have been studied using the linear interpolation method [26–31] with the augmented def2-TZVPP basis sets. Molecular geometries were analyzed with the help of the MacMolPlt [32] and MOLDEN [33] graphical programs.

3. Results and discussion

3.1. Morphological analysis of S-CDs@cis-Pt and N-CDs@cis-Pt

The morphology of hydrothermally synthesized and modified S-CDs@*cis*-Pt and *N*-CDs@*cis*-Pt were studied by TEM (Fig. 1). The average size of *N*-CDs@*cis*-Pt (Fig. 1A) were between13 and 34.5 nm, being a mean sized of 20.6 nm. Most likely, the amine- and carboxylic acid organic groups on the *N*-CDs surface promote the electrostatic interactions, thus explaining the presence of aggregates in the images (Fig. 1A, *inset*). However, no agglomeration was observed in the TEM image of S-CDs@*cis*-Pt, which showed well dispersed and semi-spherical nanoparticles with a range size between 33.3 and 83.5 nm, which showed the more repetitive values comprised between 33 and 50 nm.

Both NPs exhibited high solubility and stability in water due to the nitrogen/sulfur/oxygen-containing functional groups. The XPS
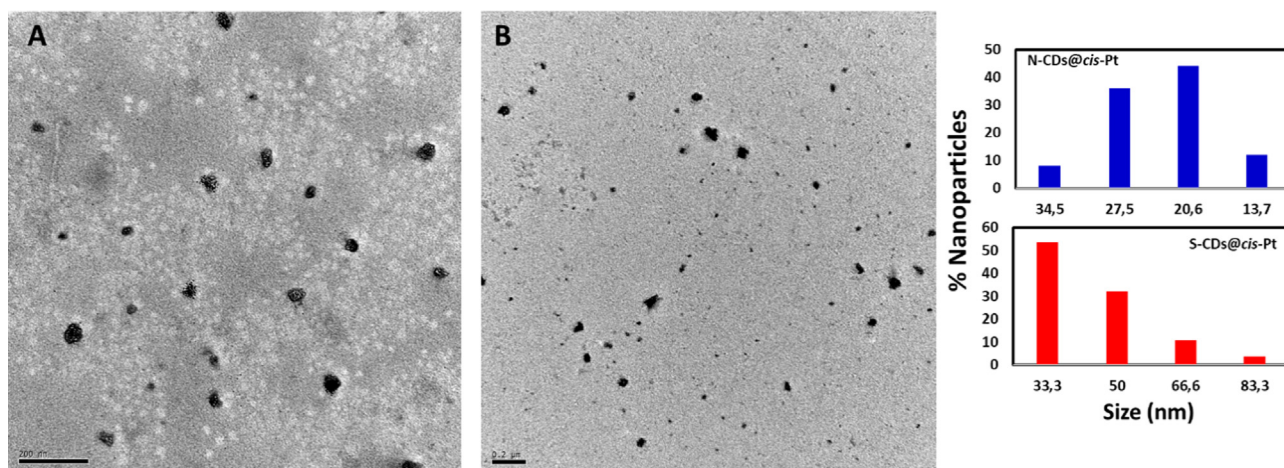
Fig. 1. TEM images of (**A**) *N*-CDs@*cis*-Pt and (**B**) S-CDs@*cis*-Pt (scale bar: 200 nm). Histograms of the as-synthesized nanoparticles.

and NMR analysis were performed to investigate their surface chemistry further.

3.2. Spectroscopic characterization of S-CDs@cis-Pt and N-CDs@cis-Pt

3.2.1. Solid and solution state NMR characterization.

Powder formulations containing functionalized *cis*-Pt samples with either S-CDs or *N*-CDs were studied by *ss*-NMR spectroscopy. The [1]H-MAS spectrum obtained at a MAS rate of 35 kHz for the pure *cis*-Pt sample showed the main broadband at ^{1}H chemical shift (δ ^{1}H) of 4.06 ppm with low intensity and broad shoulder at six ppm, which was assigned to free water molecules and the H atoms belonging to NH_3 ligands of the drug, respectively (Fig. 2). This broadband implies an amorphous state for pure *cis*-Pt. Due to the poor resolution obtained by the ^{1}H-MAS *ss*-NMR spectrum, we performed [195]Pt NMR experiments for *cis*-Pt and the S-CDs@*cis*-Pt and *N*-CDs@*cis*-Pt dissolved in D_2O. The most important finding is that the Pt signal shifts from −2165.8 ppm in the pure drug to −1677.8 and −1631.3 ppm for the S- and *N*-CDs@*cis*-Pt formulations, respectively (Fig. 2). The single [195]Pt NMR signal obtained in S and *N*-CDs@*cis*-Pt nanocomposites indicates homogeneity in chemical composition (*i.e.* occupation of all available places on the CDs surface with *cis*-Pt). The chemical shift observed at high frequencies in the [195]Pt NMR spectra of S-CDs@*cis*-Pt and

N-CDs@*cis*-Pt suggests the chemical interaction between the functional groups of CDs with Pt. Moreover, *ss*-NMR measurements on the S-CDs@*cis*-Pt and *N*-CDs@*cis*-Pt particles demonstrate that the drug was well dispersed within the CDs structures. However, the exact type of bond between Pt and the surface of CDs cannot be determined [34], by these NMR techniques applied.

The [1]H-MAS spectra for S-CDs@*cis*-Pt and *N*-CDs@*cis*-Pt were different from the spectra of free CDs (Fig. 2, and in *Suppl. Information* Figure S1 and S2). The NMR assignment for the ^{1}H signals has previously been reported [35]. Notably, the [1]H-signals corresponding to adsorbed water molecules (strongly and weakly adsorbed, SAW and WAW, respectively) [36,37] were only slightly affected by the incorporation of *cis*-Pt molecules in the formulation. On the other hand, the ^{1}H NMR signals of the polymeric content, in which the S-CDs or *N*-CDs are dispersed, were highly affected by the *cis*-Pt binding. Specifically, the ^{1}H linewidth corresponding to the hydrogen atoms of the methylene and the pyrrolidine-2-one cyclic system were the most affected signals in S-CDs and *N*-CDs samples, respectively (Figures S1 and S2).

Moreover, the contribution of the NH_3 ligands can be observed at 5–8 ppm for the *N*-CDs@*cis*-Pt sample since this sample does not contain aromatic ^{1}H signals. On the other hand, S-CDs@*cis*-Pt was difficult to analyze due to the contribution of the hydrogen atoms in the aromatic ring of the CDs-polymeric structure (δ
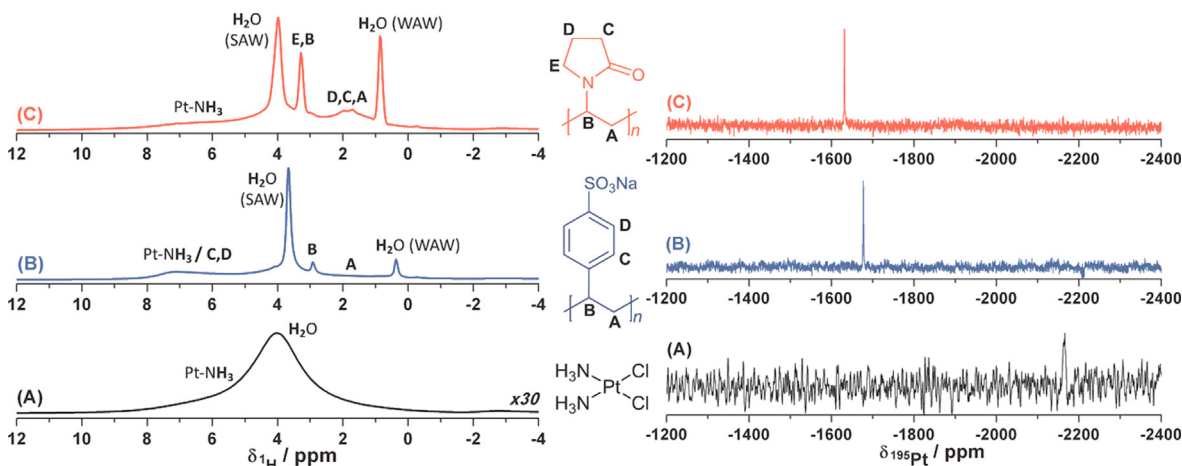

Fig. 2. (**A**) ^{1}H-MAS (@35 kHz) *ss*-NMR (left column) and [195]Pt solution-state NMR spectra in D_2O (right column) for the pure *cis*-Pt (**B**) S-CDs@*cis*-Pt and (**C**) *N*-CDs@*cis*-Pt. Legend to individual signal is given in formulae.

[1]H = 7.2 ppm). However, an increment of the ^{1}H signal can be clearly observed at a δ [1]H = 4–6 ppm, which might arise from NH$_3$ ligands in the *cis*-Pt (Figure 2 and S1).

In the ^{13}C CP-MAS experiments, the intensity of resonance signals in the ^{13}C dimension was reduced, and the *cis*-Pt content increased in the powder formulations, affecting, to some extent, the polarization of the ^{13}C nuclei. The latter phenomenon explains signal intensities in functionalized samples evaluated under the same experimental conditions (Figures S1 and S2).

When the S-CDs@*cis*-Pt and *N*-CDs@*cis*-Pt formulations were dissolved in D$_2$O, the chemical shift observed in the [195]Pt line in both samples indicates that the coordination sphere for Pt, which is changed after binding to CDs, remains unaltered in solution. Besides, the ^{1}H- and ^{13}C NMR signals arising from the S-CDs and *N*-CDs dissolved in D$_2$O were recovered and well-resolved compared to the *ss*-NMR (Figures 2, S1 and S2). This is, however, expected, if one considers changes in the chemical environment, which affect the molecular organization of the solid and reduce the paramagnetic effects of Pt centers in comparison with the solid state (Figures S3 and S4). Moreover, the interaction between *cis*-Pt and the *N*-CDs in the ^{1}H *ls*-NMR spectrum was evidenced through the shift of the hydrogen atoms from $\sim$ 3.6 ppm to 4 ppm corresponding to the > CH– group of the PVP structure located next to the *N*-atom of the amide group (Figure S4). In this case, the amide group bound to Pt induced a shift towards high-frequency values for the proton of the > CH– moiety, which indicates the coordination of the amide group in the PVP with Pt-ions along with the coordination with NH$_3$ ligands, as observed in the [1]H-MAS spectrum (Fig. 2). This NMR shift was also observed in polyethyleneimine segments bounded to Au^{3+} ions in D$_2$O solutions [38]. Likewise, the surface sulfonate functional groups from *poly*(4-styrene sulfonate at S-CDs) have the potential to establish a coordinative bond with the Pt already bound to NH$_3$ ligands. Based on the obtained information from the NMR experiments, the interaction of NPs with *cis*-Pt can be illustrated as presented in Fig. 3. *Cis*-Pt is bound to the surface of the CDs nanoparticles, allowing the possible further delivery in the treatment of cancer cells.

3.3. MALDI TOF MS analysis

MALDI TOF mass spectrometry has been proven to be a suitable method for analyzing the surface modification of carbon dots nanoparticles, as reported previously [39]. Therefore, we have applied this method to confirm *cis*-Pt binding for the surface of S-CDs, *N*-CDs. Both were analyzed with the assistance of traditional organic matrices, such as 2,5-DHB and CHCA, but also without a matrix, in a so-called LDI mode. The LDI analysis was possible thanks to the optical properties of CDs, which absorb in the UV range and can be substrates for LDI TOF mass spectrometric detection of various species [40]. In the spectra acquired without a matrix, only the signals arising from the surface modifiers of CDs are detectable. Among them, there are signals, which arise from unbound cisplatin (not indicated in the figure) and those, which arise from the *cis*-Pt bound to either PVP (Figure S5A) or PSS (Figure S5B). Each signal represents a group of signals due to a high number of Pt-isotopes, which form a characteristic pattern. Therefore, signals are indicated according to their starting and terminal positions. *Cis*-Pt-containing ions are generated by binding one cisplatin molecule to either monomer, dimers, or trimers of PVP or PSS (Cf. Table 1 for signal position and identity). It is possible that dimers or trimers of PVP and PSS are formed in the gas phase after the process of desorption/ionization and that only one cisplatin molecule is bound per PVP and PSS on the surface of CDs. Also, for the interaction of cisplatin with PVP or PSS, the loss of labile chloride ligand is required.

3.4. Computational approach

In Fig. 3, the schematic presentation of the interactions established between S-Cs and *N*-CDs and *cis*-Pt is given. This model was based on the results of NMR spectroscopy. However, for the computational approach, selected and simplified models, considering only hydrogen bonds was applied to make calculations more feasible.

3.4.1. Structural model

Given that (**i**) CDs consist of nanometer-sized carbon core surrounded by amorphous carbon frames, and that (**ii**) *N*-CDs and S-CDs are synthesized by attaching different chemical substituents to the surfaces. Amide (–CONH$_2$), amine (–CH$_2$NH$_2$) or carboxylate (–COO) groups were attached to the surface of *N*-CDs and sulfonic (-SO$_3$) groups for S-CDs [16]. The models applied for studying the interaction of *cis*-Pt with such functionalized carbon nanoparticles are given in Scheme 1.
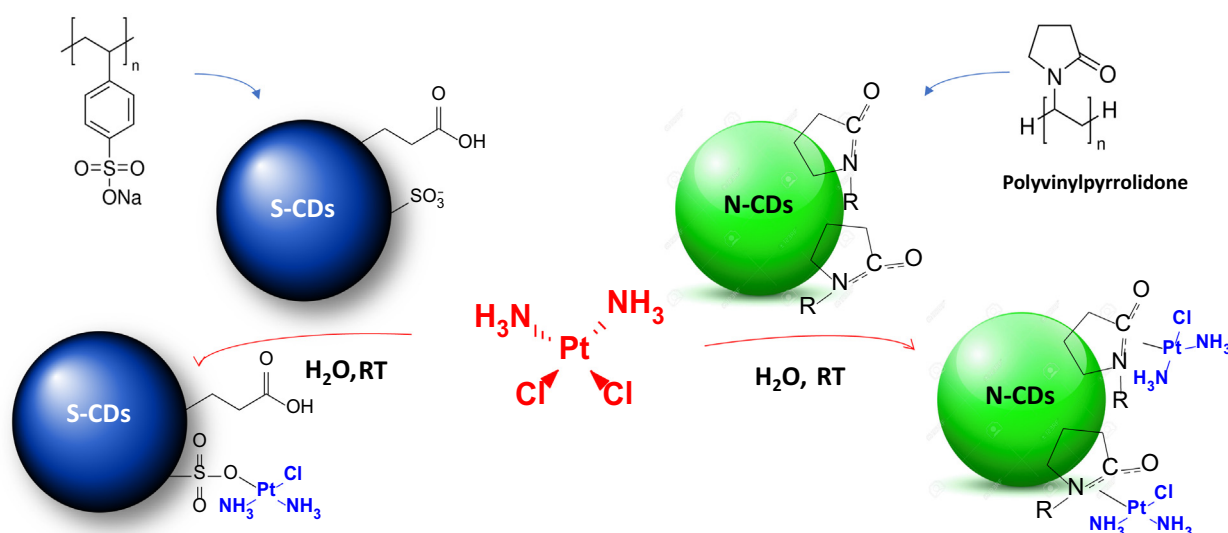

Fig. 3. Schematic representation of the surface functionalization of S-CDs@*cis*-Pt (left) and *N*-CDs@*cis*-Pt (right).

Table 1

The signal position and identity of signals are indicated in Figure S5A-B. For ease of interpretation, only the signals arising from cisplatin binding to a polymer, either polyvinylpyrrolidone (PVP) or polystyrene-sulfonate, are indicated in the spectra and listed in Table 1.

Position, m/z	Identity
361.9–367.9	cis-Pt-Cl + PSS$_1$
377.1–382.1	cis-Pt-2Cl + PVP + H
379.8–385.8	cis-Pt-Cl + PSS$_1$-H + Na
452.1–456.1	cis-Pt-2Cl + PVP$_2$ + H
559.2–572.2	cis-Pt-2Cl + PSS$_3$-H + Na
566.2–576.1	cis-Pt-2Cl + PVP$_3$ + H

The studied structures consist of different chemical moieties bound at one of the carbon atoms of the central ring of anthracene, respectively, and they agree with the models applied for studying analogous types of materials such as activated carbon acid catalysts or N doped 3D-graphene quantum dots [24,25,41,42].

3.4.2. Interaction of cisplatin with N-CDs and S-CDs.

According to the structural models proposed in Scheme 1, we have searched for the possible chemical interactions of cis-Pt with the functional groups studied in this work. Due to the complexity of potential interactions and the signal's weakness in the NMR
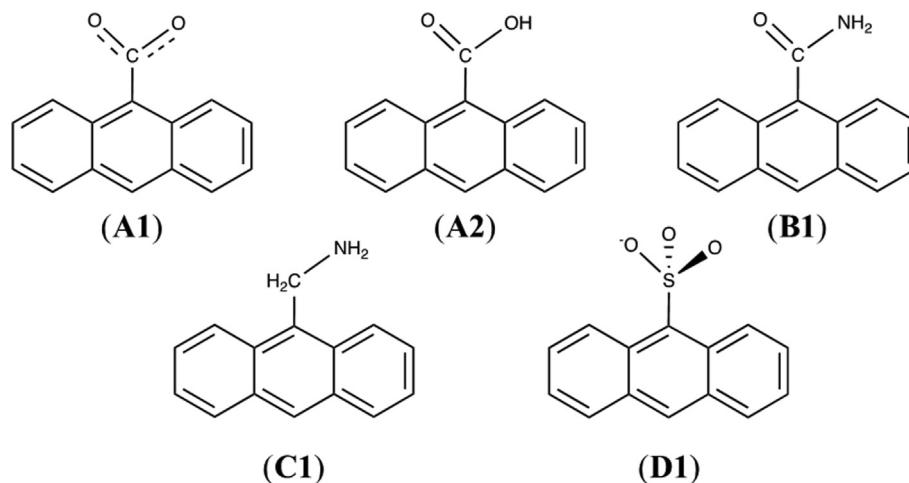
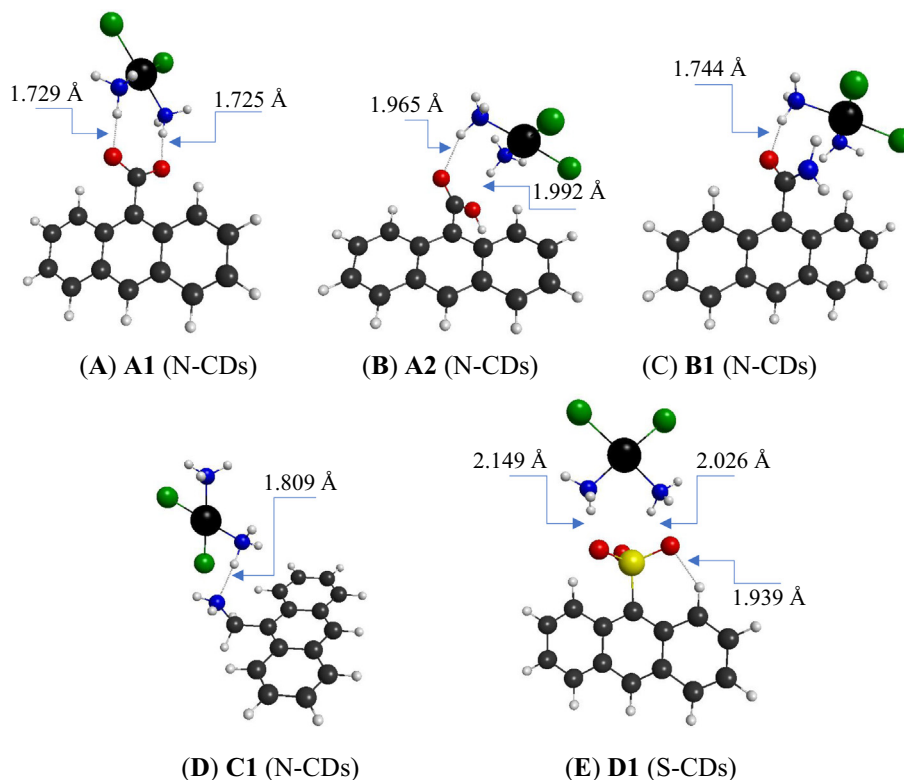**Scheme 1.** Selected models of CDs and functionalized *N*-CDs and S-CDs.

Fig. 4. CAM-B3LYP/def2-TZV optimized geometries of the complexes formed between cisplatin and *N*-CDs or S-CDs. (**A**) **A1** (–COO⁻); (**B**) **A2** (–COOH); (**C**) **B1** (–CONH$_2$); (**D**) **C1** (–CH$_2$NH$_2$); (**E**) **D1** (-SO$_3^-$).

spectra (Fig. 2), the direct interaction of donor atoms from the surface of CDs with Pt was not considered for calculations. However, after a careful search of each model, the formation of hydrogen bonds between *cis*-Pt and the corresponding substituent group of the CDs was found to stabilize the nanocomposite system (S-CDs@*cis*-Pt and.

N-CDs@*cis*-Pt). This type of interaction is noncovalent. It is established between *cis*-Pt and doped carbon dots whose origins are purely coulombic [43], leading to the formation of *cis*-Pt-CDs complexes without alteration of the molecular geometry of the drug. The binding of *cis*-Pt via hydrogen bonds, and only scarce use of the central metal ion, is essential since the drug geometry is vital for finding the biological target for *cis*-Pt. The minimum energy geometries of such complexes are depicted in Fig. 4 and Table 2 collects their reaction enthalpies (Δ_rH) and Gibbs free

energies (Δ_rG) computed at 298.15 K. The most stable complexes correspond to those ones in which the functional group (–COO⁻ and -SO₃⁻) is charged, following the big dipole moment of *cis*-Pt, which is calculated at ∼ 12 D.

The potential energy surfaces that lead to the formation of each molecular complex are represented in Figure S6; they are obtained with the linear interpolation method [26–31]. Such interpolations indicate that the potential surfaces for the formation of the complexes are barrierless; that is, the CDs act as attractors. Additionally, the model aligns with changes observed in the position of proton signals in the NMR spectra of S-CDs@*cis*-Pt and *N*-CDs@*cis*-Pt (Fig. 2).

3.5. Cell characterization: In vitro cell viability

The effect of S-CDs@*cis*-Pt and *N*-CDs@*cis*-Pt on the viability of A2780 ovarian cancer cells culture was studied, and the results are shown in Fig. 5. Two well-characterized ovarian cancer cell lines, namely cells sensitive to *cis*-Pt (A2780, Fig. 5A) and the same type of carcinoma cells, but resistant to *cis*-Pt (A2780R, Fig. 5B) were investigated. The effect of both *cis*-Pt formulations was compared to the effect of individual CDs and *cis*-Pt.

As expected, A2780 cells are sensitive to *cis*-Pt, and their viability decreases with an increasing concentration of *cis*-Pt. The achieved IC₅₀ value (the concentration of a drug that leaves 50% of cells viable) was 0.2 ± 0.002 μM, whereas S-CDs and *N*-CDs demonstrated no cytotoxicity in the tested concentration range

Table 2
CAM-B3LYP/def2-TZVPP// CAM-B3LYP/def2-TZV reaction enthalpies and Gibbs free energies to form *cis*-Pt-CDs complexes.[a]

Complex	Δ_rH	Δ	$\Delta_r E_e^c$
A1	−49.2	−38.9	−51.4
A2	−17.1	−5.8	−18.7
B1	−19.2	−7.52	−20.9
C1	−14.4	−2.40	−16.2
D1	−44.5	−32.8	−46.9

[a] Temperature: 298.15 K; energies in kcal/mol. geometries are given in Figure C1. electronic energy in kcal/mol.
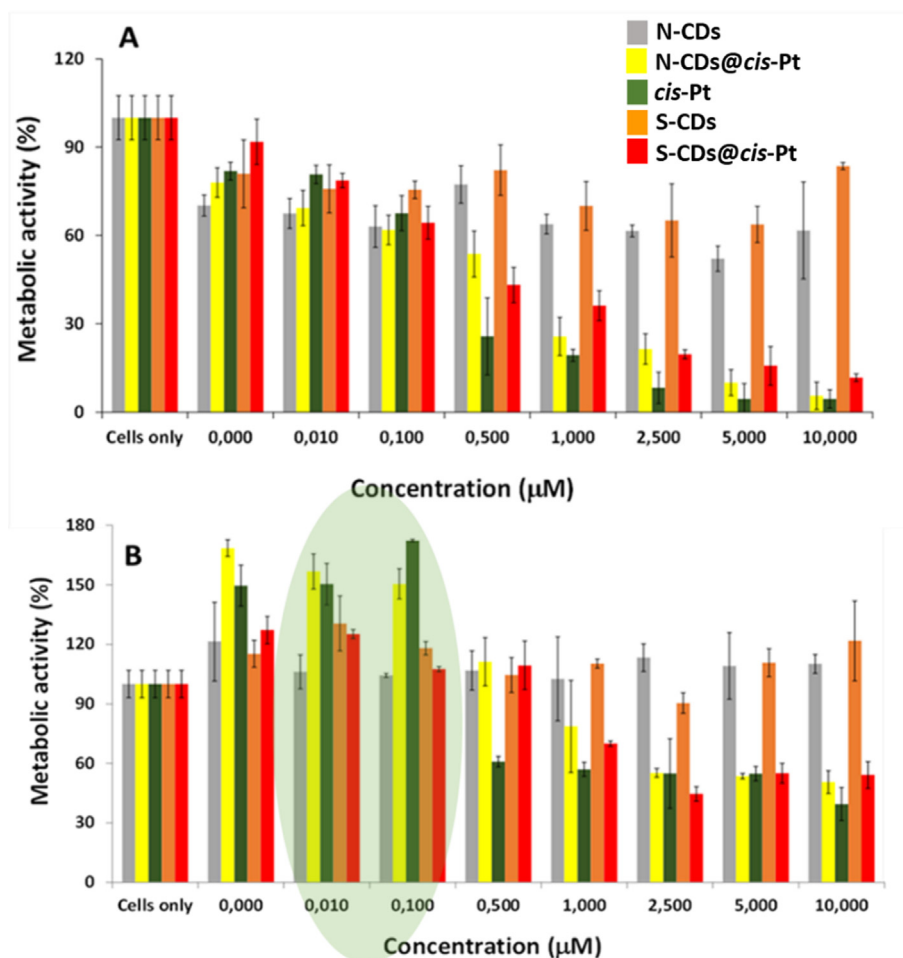

Fig. 5. Comparative metabolic activity of *cis*-Pt and the different carbon nanoparticles with the ovarian cancer cell lines (**A**) Sensitive to *cis*-Pt, A2780 and (**B**) *cis*-Pt resistant, A2780R. All concentrations are expressed as concentrations of *cis*-Pt.

(Fig. 5A). The IC$_{50}$ values obtained for S-CDs@*cis*-Pt and *N*-CDs@*cis*-Pt were 0.3 ± 0.002 and 0.5 ± 0.004 μM, respectively.

The second cell line investigated is A2780R, resistant to the treatment with *cis*-Pt, which is also confirmed by our experiment (Fig. 5B). Specifically, the IC$_{50}$ value for *cis*-Pt was not achieved within the tested concentration range. Similarly, none of CDs was cytotoxic (IC$_{50}$ > μM), whereas the combination of S-CDs@*cis*-Pt overcame *cis*-Pt resistance (achieved IC$_{50}$ value of 2.25 ± 0.01 μM). For *N*-CDs@ *cis*-Pt, IC$_{50}$ value was higher than 10 μM. In addition, at the two lowest concentrations of *cis*-Pt, namely 0.01, and 0.100 μM (highlighted with a grey bar in Fig. 5B), the formulation of *cis*-Pt with S-CDs was efficient in overcoming cell resistance to *cis*-Pt (Fig. 5B), whereas *N*-CDs showed no activity. Due to the severe side effects of *cis*-Pt administered through the circulation [4,5], it is essential to achieve an anti-tumor effect with lower concentrations of chemotherapeutic.

The formulation of S-CDs@*cis*-Pt is more efficient in killing ovarian cancer cells than *N*-CDs@*cis*-Pt since its IC$_{50}$ value in A2780 cells was lower, and in A2780R cells, it was the one that overcame the resistance to *cis*-Pt. It is speculated that the *cis*-Pt resistance of cancer cells arises from the drug accumulation in the cell and subsequent inactivation [40]. Therefore, S-CDs@*cis*-Pt overcomes the resistance might be because of the higher stability of the complex of Pt with S-donor on the surface of S-CDs, which is also obtained by computational analysis (*cf.* below), and experimentally demonstrated in previous work [41]. Compared to *N*-donors from the surface of *N*-CDs, the formulation S-CDs@*cis*-Pt, as more stable, is also less susceptible to the interaction with intracellular biomolecules that can cause accumulation of *cis*-Pt inside the cells and the neutralization. On the other hand, in A2780 cells, sensitive to *cis*-Pt, IC$_{50}$ values of S-CDs@*cis*-Pt and *N*-CDs@*cis*-Pt are somewhat higher compared to pure *cis*-Pt, which can be explained by slower exchange reactions when *cis*-Pt is bound already to donor molecules (S- and N- on the surface of CDs).

3.6. SR-FTIR analysis of A2780 and A2780R cells after treatment with S-CDs, N-CDs, and their functionalized cis-Pt derivates

To follow the mild effect of the nanomaterials on both types of cells, for the further FTIR estimation of the cellular biomacro-molecule status, we used a concentration of 0.1 μM. Fig. 6 shows the FTIR spectra obtained for A2780 (A) and A2780R cells (B): untreated, *N*-CDs treated, S-CDs treated, and cells treated with *N*-CDs@*cis*-Pt or S-CDs@*cis*-Pt and cisplatin simultaneously. The individual spectra were statistically compared using PCA analysis (Fig. 6C, D). The shape of the bands corresponding to functional groups arising from various biomolecules like nucleic acids, carbohydrates, proteins, and lipids is different and dependent on the treatment and the cell type. In A2780 cells, the most significant changes in the bio-macromolecules are induced by the treatment with *N*-CDs@*cis*-Pt concerning the fingerprint region of nucleic acids (mostly DNA).

In contrast, the most significant changes in lipid area are induced by the treatment with *N*-CDs, S-CDs, and S-CDs@*cis*-Pt (Fig. 6A,). In the case of A2780R cells, the most significant difference, compared to the control (non-treated cells), was observed after the treatment with S-CDs and S-CDs@*cis*-Pt (DNA and protein region) and an increase in the lipids-related bands after all treatment (Fig. 6B, C).
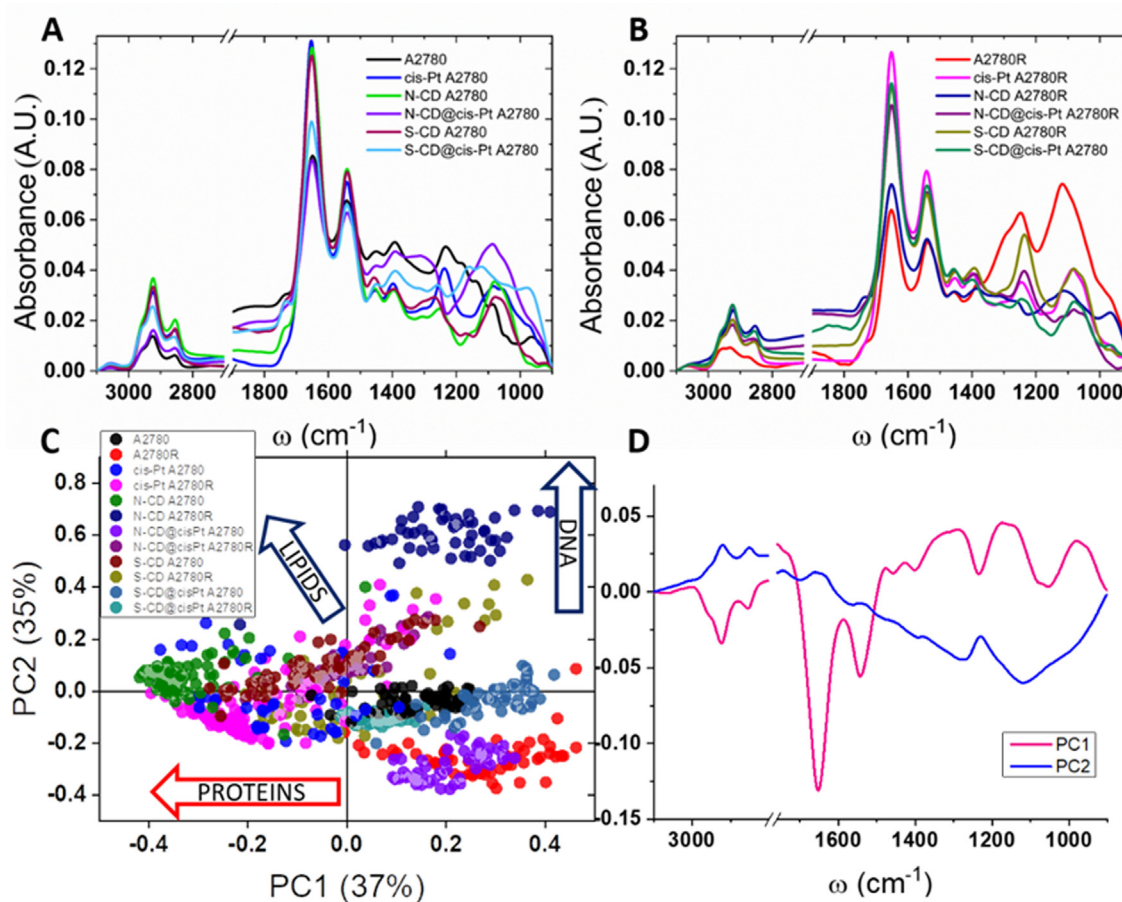

Fig. 6. (**A**) Averaged FTIR spectra of the sensitive and (**B**) *cis*-Pt resistant A2780 cells (**B**) untreated, *cis*-Pt-treated, *N*-CDs-treated, S-CDs-treated, and cells treated with *N*-CDs or S-CDs and *cis*-Pt simultaneously. Each treatment is indicated by a different color of spectra (N = 50). (**C**) The PCA score plot of two first PCA components and (**D**) contribution of individual absorbance to these components (loading plot).

The PCA, and the corresponding scatter and loadings plots are given in Fig. 6C, D and represent cell types changes according to the spectral bands' characteristics for organic compounds. The PCA score plot showed that a two-component model explains 72 % of the variability (PC1 accounted for 37 % and PC2 for 35 %). The objects in the plots were characterized as cell types and treatments, and the variables are the FTIR wavenumbers. From the loadings plots (Fig. 6D), it is possible to identify wavenumbers influential for the separation among the samples. In PC1 loadings, the dominant bands are the Amide I and II, namely the α helix spectral bands at 1653 and 1542 cm^{-1}, respectively (Fig. 6D).

Furthermore, the bands at 2924, 2852 cm^{-1} characteristic for lipids and PO$_2$ asymmetric stretch of DNA bound phosphates $\sim$ 1234 cm^{-1}are also appear in the PC1 loadings. According to the PC2, the dominant bands are vibration at 1122 cm^{-1} characteristic for C—O stretch vibration of ribose ring in RNA and PO$_2^-$ an asymmetric stretch of DNA-related phosphates at 1234 cm^{-1} [44]. Regarding the lipid changes, the main difference was observed at the 2924 cm^{-1} and 2853 cm^{-1}, bands assigned to CH$_2$ asymmetric and symmetric stretching vibrations, respectively. This increase and change in the position of CH$_2$ bands pointed toward shorter lipids molecules formation and change in membrane fluidity [45] of treated A2780 and A2780R cells.

Based on the positions of the scores along PC1 and their related loadings, there was a decrease in lipids'- and proteins'- bands (corresponding to intensities of their characteristic spectral bands), in the direction shown by arrows in Fig. 6C with the most significant change in N-CDs, treated A2780 and N-CDs@cis-Pt-treated A2780R cells, as well as the cis-Pt-treated A2780 and A2780R cells, in comparison to the control cells (both A2780, A2780R). A similar effect was displayed in the S-CDs@cis-Pt-treated A2780 and N-CDs@cis-Pt-treated A2780 cells. Based on the positions of the scores along PC2 (Fig. 6C) and their related loadings, there was a decrease in the phosphate band corresponding to the DNA in the direction indicated by an arrow in Fig. 6C. Here, a decrease in DNA (and RNA) bands was highest for N-CDs treated A2780R cells and lowest after treating A2780 cells with N-CDs@cis-Pt. This result might indicate the suitability of N-CDs as the carrier that can reach the nucleus and the target molecules (DNA) that are a primary target for the action of cis-Pt, as discussed above. Besides, the negative effect on DNA bands has also the S-CDs on both cells A2780 and A2780R. In addition, the N-CDs effect on DNA in A2780 cells is notable, but on the other hand, the proteins were also significantly changed.

In summary, the PCA shows that both S-CDs and N-CDs affect the A2780 cells by inducing changes in all three classes of biomolecules, which is visible as the change in the averaged spectra (Fig. 6A, B). It was noted that the DNA band decreased in intensities of the characteristic spectral bands of the treated cells compared to the controls. The results also show that proteins, lipids, and DNA are most affected by the treatments, which may be a part of the cancer cells' damage. The effect of S-CDs@cis-Pt and N-CDs@cis-Pt is stronger than treatment with cis-Pt alone, for both sensitive and cis-Pt resistant cells, regarding the decrease in cellular proteins or lipids/membranes- bands, as shown by FTIR. Although they might not be the primary target for cis-Pt, proteins and lipids may also contribute to cancer cell death through signaling pathways. Having in mind that lipids emerge as new target molecules for cancer treatment [45] and that cis-Pt might be activated after the interaction with the phospholipids in the inner membrane [43], the combination of this drug with S-CDs and N-CDs is promising in the adenocarcinoma treatment.
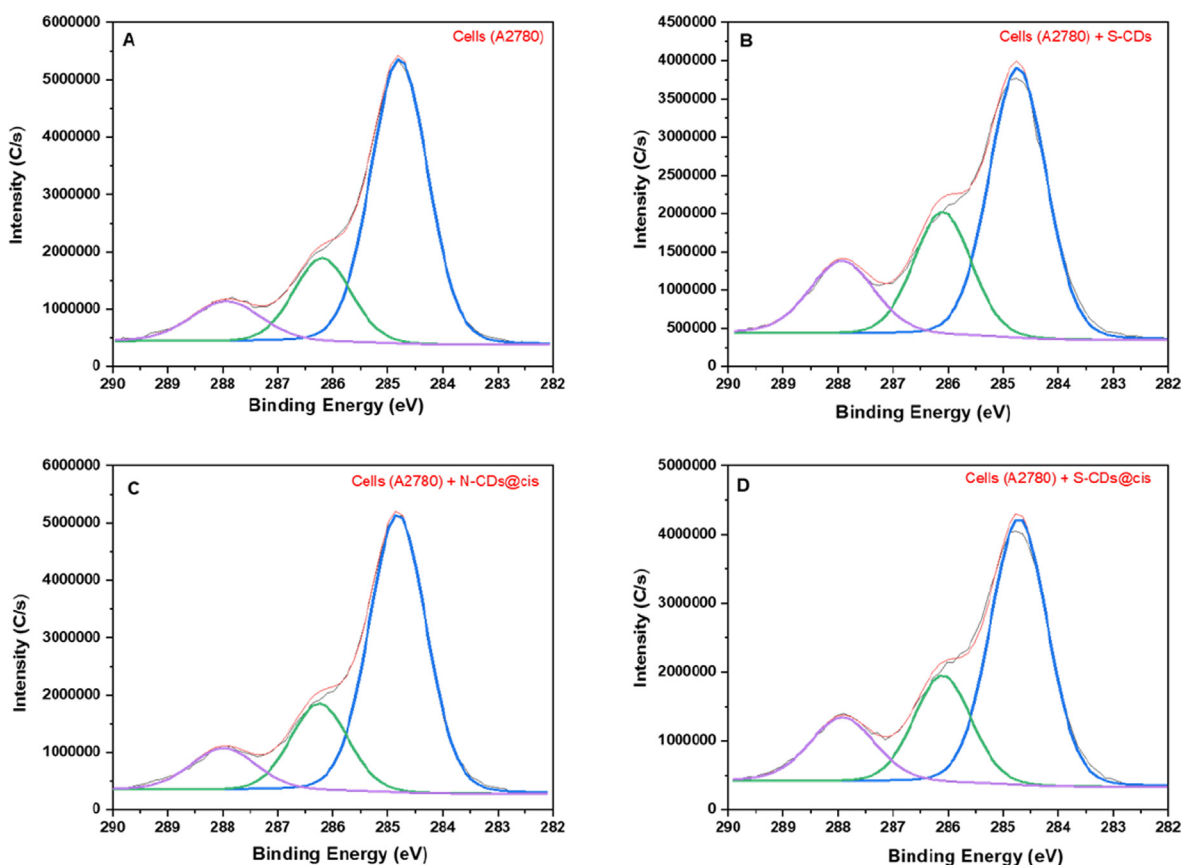

Fig. 7. High-resolution C 1 s XPS spectra for (**A**) Control A2780 cells and treated with (**B**) S-CDs, (**C**) N-CDs@cis-Pt and (**D**) S-CDs@ cis-Pt.

Table 3
Area contribution (%) for the C 1 s.

	C—C/C—H	C—O/C—N	O-C=O
Position (eV):	284.8	286.15	288.1
A2780-cells	67.76	19.98	12.27
A2780-S-CDs	56.27 (17.0 %)*	25.63 (28.3 %)*	18.10 (29.9 %)*
A2780-S-CDs@Cisplatin	59.20 (12.6 %)*	23.77 (19.0 %)*	17.02 (23.7)*
A2780-*N*-CDs@Cisplatin	66.96	20.97	12.07 (***N*-C=O**)**

* In parenthesis, the decreasing (red) and increasing (blue) of the signal compared with C—C/C—H.
** Is assumed that this contribution is comprised of this group.

Table 4
Atomic concentration (%) of the obtained S-CDs@*cis*-Pt and *N*-CDs@*cis*-Pt.

	C	O	N		Cl	Pt
***N*-CDs**	75.4	14.3	10.3			
***N*-CDs@*cis*-Pt**	67.4	13.9	13.3		3.1	2.3
			S	Na		
S-CDs	17	46.5	10.7	25	12.8	
S-CDs@*cis*-Pt	31.0	31.1	8	6	6.7	4.4

3.7. XPS analysis. Interaction of S-CDs@cis-Pt and N-CDs@cis-Pt with A2780 cells

To further understand the interaction of *cis*-Pt with S-CDs and *N*-CDs with A2780 cells, we analyzed the XPS spectra of cells treated in the same way described in the previous section. Fig. 7 shows the XPS spectra of A2780 cells, whereas similar spectra were also acquired for A2780R cells. In Fig. 7A, the spectra of A2780 cells (non-treated) are given, and the main component is assigned to the adventitious carbon signal (C—C/C—H) at 284.8 eV, with which we will be comparing the other signals. These signals decreased by 17 and 12.6 % (Table 3) after treating cells with S-CDs or S-CDs@*cis*-Pt. This result can be explained by the carbonyl groups covering the CDs. The XPS can detect NPs on the surface of different cells and their interactions with functional groups [46].

The treatment of A2780 cells with *N*-CDs@*cis*-Pt does not affect the chemical composition of cells (Fig. 7C). The ratio for both samples increased 28.3 (Fig. 7B) and 19.0 % (Fig. 7D) for C—O/C—N (at 286.2 eV) and 29.2 (Fig. 7B) and 23.7 % (Fig. 7D) O-C=O/*N*-C=O signals (at 287.9 eV) [47]. This is a correlation with the FTIR spectra, in which the most intense interaction is observed in the protein vibrations (Amide I and II) (Fig. 6). The most substantial interaction of nanocomposites with S-CDs is observed with lipids and proteins on the cell surface. On the other hand, the interaction of NPs containing *N*-CDs was not detectable by this method, which agrees with FTIR data, *i.e.* the interaction with nucleic acids, inside the cells.

The XPS analysis of the raw *cis*-Pt, *N*-CDs@*cis*-Pt and S-CDs@*cis*-Pt is given in Figure S7A-C, whereas the high-resolution C 1 s, N 1 s and O1s spectra of *N*-CDs@*cis*-Pt and S-CDs@*cis*-Pt are depicted in Figure S8. The surface chemical composition (in atomic concentration, %) of the obtained raw S-CDs@*cis*-Pt and *N*-CDs@*cis*-Pt was performed by XPS analysis (Table 4). This analysis is interesting because it showed the high surface content of O in S-CDs@*cis*-Pt, explained by the high content of sulfonic groups, even after reaction with *cis*-Pt.

4. Conclusions

Based on the previous reports, which focus on the administration of *cis*-Pt using carbon nanoparticles [7,48–51], the present work demonstrates that S-CDs@*cis*-Pt and *N*-CDs@*cis*-Pt composites can be used as a *cis*-Pt delivery systems to treat ovarian cancer adenocarcinoma cells A2780. The use S-CDs and *N*-CDs functional-

ized with *cis*-Pt helps to overcome metallo drug resistance, one of the major problems in chemotherapy [1,2]. The main features of the surface characterization of both obtained systems, S-CDs@*cis*-Pt and *N*-CDs@*cis*-Pt, were observed by ss- and ls-NMR studies which confirmed the homogeneity of *cis*-Pt distribution on the surface of both composites. Other spectroscopic techniques applied in this work also confirm the successful surface modification of S-CDs and *N*-CDs through a hydrogen bond between the NH_2 group of *cis*-Pt and the NH_2 group of *N*-CDs on the one hand, and the RSO_3^- group of S-CDs with the same group of *cis*-Pt. In this sense, NMR measurements also detect the direct interaction of N and S-donors on the surface of *N*-CDs and S-CDs with Pt ion, respectively. SR-FTIR analysis showed the effect of *N*-CDs as potential carrier for *cis*-Pt, but also as single NPs directly affect DNA in A2780 resistant cells. XPS confirms that the most substantial interactions are observed with S-CDs with lipids and proteins on the cell surface, by observing the C 1 s core level spectra, and probably do not enter the nucleus and thus do not affect DNA. All these results strongly suggest a high potential of the S-CDs and *N*-CDs as carriers for *cis*-Pt drug delivery; the investigated system might also be adopted for other types of transition metal complexes.

CRediT authorship contribution statement

Tanja Dučić: Conceptualization, Formal analysis, Writing – original draft, Writing – review & editing. **Carla S. Alves:** Methodology, Resources, Formal analysis, Writing – review & editing. **Željko Vučinić:** Formal analysis, Writing – review & editing. **Juan M. Lázaro-Martínez:** Formal analysis, Writing – review & editing. **Marijana Petković:** Methodology, Formal analysis, Writing – review & editing. **Juan Soto:** Formal analysis, Writing – review & editing. **Dragosav Mutavdžić:** Formal analysis, Writing – review & editing. **M. Valle Martínez de Yuso:** Formal analysis, Writing – review & editing. **Ksenija Radotić:** Conceptualization, Resources, Formal analysis, Writing – original draft, Writing – review & editing. **Manuel Algarra:** Conceptualization, Resources, Formal analysis, Writing – original draft, Writing – review & editing.

Declaration of Competing Interest

The authors declare that they have no known competing financial interests or personal relationships that could have appeared to influence the work reported in this paper.

Acknowledgments

Appendix A. Supplementary data

Supplementary data to this article can be found online at https://doi.org/10.1016/j.jcis.2022.05.005.

References

[1] C.M. Beaufort, J.C.A. Helmijr, A.M. Piskorz, M. Hoogstraat, K. Ruigrok-Ritstier, N. Besselink, M. Murtaza, W.F.J. van IJcken, A.A.J. Heine, A. Smid, M.J. Koudijs, J.D. Brenton, E.M.J.J. Berns, J. Helleman, R. Pearson, Ovarian cancer cell line panel (OCCP): clinical importance of in vitro morphological subtypes, PLOS ONE. 9 (9) (2014) e103988, https://doi.org/10.1371/journal.pone.0103988.

[2] H. Bai, D. Cao, J. Yang, M. Li, Z. Zhang, S. Shen, Genetic and epigenetic heterogeneity of epithelial ovarian cancer and the clinical implications for molecular targeted therapy, J. Cell. Mol. Med. 20 (4) (2016) 581–593, https://doi.org/10.1111/jcmm.12771.

[3] J.Y. Lee, J.K. Yoon, B. Kim, S. Kim, M.A. Kim, H. Lim, D. Bang, Y.S. Song, Tumor evolution and intratumor heterogeneity of an epithelial ovarian cancer investigated using next-generation sequencing, BMC Cancer. 15 (2015) 85, https://doi.org/10.1186/s12885-015-1077-4.

[4] D.-W. Shen, L.M. Pouliot, M.D. Hall, M.M. Gottesman, D.R. Sibley, Cisplatin resistance: a cellular self-defense mechanism resulting from multiple epigenetic and genetic changes, Pharmacol. Rev. 64 (3) (2012) 706–721, https://doi.org/10.1124/pr.111.005637.

[5] S. Dasari, P.B. Tchounwou, Cisplatin in cancer therapy: molecular mechanisms of action, Eur. J. Pharmacol. 740 (2014) 364–378, https://doi.org/10.1016/j.ejphar.2014.07.025.

[6] G. Chen, Y. Yang, Q. Xu, M. Ling, H. Lin, W. Ma, R. Sun, Y. Xu, X. Liu, N. Li, Z. Yu, M. Yu, Self-Amplification of Tumor Oxidative Stress with Degradable Metallic Complexes for Synergistic Cascade Tumor Therapy, Nano Lett. 20 (11) (2020) 8141–8150, https://doi.org/10.1021/acs.nanolett.0c0312710.1021/acs.nanolett.0c03127.s001.

[7] Y. Yang, Y. Yu, H. Chen, X. Meng, W. Ma, M. Yu, Z. Li, C. Li, H. Liu, X. Zhang, H. Xiao, Z. Yu, Illuminating Platinum Transportation while Maximizing Therapeutic Efficacy by Gold Nanoclusters via Simultaneous Near-Infrared-I/II Imaging and Glutathione Scavenging, ACS Nano. 14 (10) (2020) 13536–13547, https://doi.org/10.1021/acsnano.0c0554110.1021/acsnano.0c05541.s001.

[8] W. Ma, Q. Chen, W. Xu, M. Yu, Y. Yang, B. Zou, Y.S. Zhang, J. Ding, Z. Yu, Self-targeting visualizable hyaluronate nanogel for synchronized intracellular release of doxorubicin and cisplatin in combating multidrug-resistant breast cancer, Nano Res. 14 (3) (2021) 846–857, https://doi.org/10.1007/s12274-020-3124-y.

[9] Y. Yang, X. Liu, W. Ma, Q. Xu, G. Chen, Y. Wang, H. Xiao, N. Li, X.-J. Liang, M. Yu, Z. Yu, Light-activatable liposomes for repetitive on-demand drug release and immunopotentiation in hypoxic tumor therapy, Biomaterials. 265 (2021) 120456, https://doi.org/10.1016/j.biomaterials.2020.120456.

[10] H. Li, X. He, Y. Liu, H. Huang, S. Lian, S.-T. Lee, Z. Kang, One-step ultrasonic synthesis of water-soluble carbon nanoparticles with excellent photoluminescent properties, Carbon 49 (2) (2011) 605–609, https://doi.org/10.1016/j.carbon.2010.10.004.

[11] S. Baker, G. Baker, Luminescent carbon nanodots: emergent nano-lights, Angew. Chem Int Ed 49 (38) (2010) 6726–6744, https://doi.org/10.1002/anie.200906623.

[12] M. Algarra, M. Pérez-Martín, M. Cifuentes-Rueda, J. Jiménez-Jiménez, J.C.G. Esteves da Silva, T.J. Bandosz, E. Rodríguez-Castellón, J.T. López Navarrete, J. Casado, Carbon dots obtained using hydrothermal treatment of formaldehyde,

[13] S.-T. Yang, Li. Cao, P.G. Luo, F. Lu, X. Wang, H. Wang, M.J. Meziani, Y. Liu, G. Qi, Y.-P. Sun, Carbon dots for optical imaging in vivo, J Am Chem Soc. 131 (32) (2009) 11308–11309, https://doi.org/10.1021/ja904843x.

[14] T. Feng, H.J. Chua, Y. Zhao, Carbon Dot-Mediated Co-Administration of Chemotherapeutic Agents for Reversing Cisplatin Resistance in Cancer Therapy, Chem. Nano Mat. 4 (8) (2018) 801–806, https://doi.org/10.1002/cnma.201700367.

[15] M. Algarra, B.B. Campos, R. Radotić, D. Mutavdžić, T. Bandosz, J. Jiménez-Jiménez, E. Rodriguez-Castellón, J.C.G. Esteves da Silva, Luminescent carbon nanoparticles: effects of chemical functionalization, and evaluation of Ag^+ sensing properties, J Mater Chem A 2 (2014) 8342–8351, https://doi.org/10.1039/C4TA00264D.

[16] N.A. Travlou, D.A. Giannakoudakis, M. Algarra, A.M. Labella, E. Rodríguez-Castellon, T.J. Bandosz, S and N-doped carbon quantum dots: Surface chemistry dependent antibacterial activity, Carbon 135 (2018) 104–111, https://doi.org/10.1016/j.carbon.2018.04.018.

[17] B.M. Fung, A.K. Khitrin, K. Ermolaev, An Improved Broadband Decoupling Sequence for Liquid Crystals and Solids, J. Magn. Reson. 142 (1) (2000) 97–101, https://doi.org/10.1006/jmre.1999.1896.

[18] T. Dučić, M. Ninkovic, I. Martínez-Rovira, S. Sperling, V. Rohde, D. Dimitrijević, G.V. Jover Mañas, L. Vaccari, G. Birarda, I. Yousef, Live-cell synchrotron-based ftir evaluation of metabolic compounds in brain glioblastoma cell lines after riluzole treatment, Anal. Chem. 94 (4) (2022) 1932–1940, https://doi.org/10.1021/acs.analchem.1c0207610.1021/acs.analchem.1c02076.s001.

[19] M. Matijević, Đ. Nakarada, X. Liang, L. Korićanac, L. Rajsiglova, L. Vannucci, M. Nešić, M. Vranješ, M. Mojović, L. Mi, I. Estrela-Lopis, J. Böttner, Z. Šaponjić, M. Petković, M. Stepić, Biocompatibility of TiO_2 prolate nanospheroids as a potential photosensitizer in therapy of cancer, J Nanopart Res. 22 (2020) 175. https://doi.org/10.1007/s11051-020-04899-3.).

[20] T. Yanai, D.P. Tew, N.C. Handy, A new hybrid exchange-correlation functional using the Coulomb-attenuating method (CAM-B3LYP), Chem. Phys. Lett. 393 (1-3) (2004) 51–57, https://doi.org/10.1016/j.cplett.2004.06.011.

[21] F. Weigend, R. Ahlrichs, Balanced basis sets of split valence, triple zeta valence and quadruple zeta valence quality for H to Rn: Design and assessment of accuracy, Phys. Chem. Chem. Phys. 7 (2005) 3297–3305, https://doi.org/10.1039/B508541A.

[22] F. Weigend, Accurate Coulomb-fitting basis sets for H to Rn, Phys. Chem. Chem. Phys. 8 (2006) 1057–1065, https://doi.org/10.1039/B515623H.

[23] Gaussian 16, Revision A.03, M. J. Frisch et al. Gaussian, Inc., Wallingford CT, 2016.

[24] D. Houdova, J. Soto, R. Castro, J. Rodrigues, M.S. Pino-Gonzalez, M. Petkovic, T.J. Bandosz, M. Algarra, Chemically heterogeneous carbon dots enhanced cholesterol detection by MALDI TOF mass spectrometry, J. Coll. Interf. Sci. 591 (2021) 373–383, https://doi.org/10.1016/j.jcis. 2021.02.004.

[25] M. Nunes, I. Popovic, E. Abreu, D. Maciel, J. Rodrigues, J. Soto, M. Algarra, M. Petkovic. Detection of Ru potential metallodrug in human urine by MALDI-TOF mass spectrometry: Validation and options to enhance the sensitivity. Talanta 222 (2021) 121551. https://doi.org/ 10.1016/J.TALANTA.2020.121551.

[26] J. Soto, J.C. Otero, F.J. Avila, D. Peláez, Conical intersections and intersystem crossings explain product formation in photochemical reactions of aryl azides, Phys. Chem. Chem. Phys. 21 (5) (2019) 2389–2396, https://doi.org/10.1039/C8CP06974C.

[27] J. Soto, J.C. Otero, Conservation of El-Sayed's Rules in the Photolysis of Phenyl Azide: Two Independent Decomposition Doorways for Alternate Direct Formation of Triplet and Singlet Phenylnitrene, J. Phys. Chem. A 123 (42) (2019) 9053–9060, https://doi.org/10.1021/acs.jpca.9b0691510.1021/acs.jpca.9b06915.s001.

[28] D. Aranda, F.J. Avila, I. López-Tocón, J.F. Arenas, J.C. Otero, J. Soto, An MS-CASPT2 study of the photodecomposition of 4-methoxyphenyl azide: role of internal conversion and intersystem crossing, Phys. Chem. Chem. Phys. 20 (11) (2018) 7764–7771, https://doi.org/10.1039/C8CP00147B.

[29] D. Peláez, J.F. Arenas, J.C. Otero, J. Soto, Dependence of N-nitrosodimethylamine Photodecomposition on the Irradiation wavelength: Excitation to the S-2 state as a Doorway to the Dimethylamine Radical Ground-State Chemistry, J. Org. Chem. 72 (2007) 4741–4749, https://doi.org/10.1039/C8CP00147B.

[30] J. Soto, D. Peláez, J.C. Otero, F.J. Ávila, J.F. Arenas, Photodissociation Mechanism of Methyl Nitrate. A study with the Multistate Second-Order Multiconfigurational Perturbation Theory, Phys. Chem. Chem. Phys. 11 (2009) 2631–2639, https://doi.org/10.1039/B820646E.

[31] D. Peláez, J.F. Arenas, J.C. Otero, J. Soto, A complete active space self-consistent field study of the photochemistry of nitrosamine, J. Chem. Phys. 125 (16) (2006) 164311, https://doi.org/10.1063/1.2360259.

[32] B.M. Bode, M. S. Gordon. MacMolPlt: A graphical user interface for GAMESS. J. Mol. Graphics Modell., 16 (1998) 133-138. https://doi.org/10.1016/s1093-3263(99)00002-9.

[33] G. Schaftenaar, J.H. Noordik, Molden: a pre- and post-processing program for molecular and electronic structures, J. Comput. Aided Mol. Des. 14 (2000) 123–134, https://doi.org/10.1023/A:1008193805436.

[34] B.M. Still, P.G.A. Kumar, J.R. Aldrich-Wright, W.S. Price, [195]Pt NMR - Theory and application, Chem. Soc. Rev. 36 (2007) 665–686, https://doi.org/10.1039/B606190.

[35] N.A. Travlou, M. Algarra, C. Alcoholado, M. Cifuentes-Rueda, A.M. Labella, J.M. Lázaro-Martínez, E. Rodriguez-Castellon, T.J. Bandosz, CQDs-surface

chemistry-dependent Ag release governs the high antibacterial activity of AgMOF composites, ACS Appl. Bio Mater. 1 (2018) (2018) 693–707, https://doi.org/10.1021/acsabm.8b00166.

[36] A.F. Crespi, A.J. Byrne, D. Vega, A.K. Chattah, G.A. Monti, J.M. Lázaro-Martínez, Generation and Stability of the gem-Diol Forms in Imidazole Derivatives Containing Carbonyl Groups. Solid-State NMR and Single-Crystal X-ray Diffraction Studies, J. Phys. Chem. A 122 (2) (2018) 601–609.

[37] E.E. Wilson, A. Awonusi, M.D. Morris, D.H. Kohn, M.M.J. Tecklenburg, L.W. Beck, Three structural roles for water in bone observed by solid-state NMR, Biophys. J. 90 (10) (2006) 3722–3731, https://doi.org/10.1529/biophysj.105.070243.

[38] Lázaro-Martínez, J. M.; Byrne, A. J.; Rodríguez-Castellón, E.; Manrique, J. M.; Jones, L. R.; Campo Dall' Orto, V. Linear Polyethylenimine-Decorated Gold Nanoparticles: One-Step Electrodeposition and Studies of Interaction with Viral and Animal Proteins. Electrochim. Acta 2019, 301, 126-135. https://doi.org/10.1016/j.electacta.2019.01.154.

[39] A. Khanam, S.K. Tripathi, D. Roy, M. Nasim, A facile and novel synthetic method for the preparation of hydroxyl capped fluorescent carbon nanoparticles, Colloids Surf. B Biointerfaces 102 (2013) 63–69, https://doi.org/10.1016/j.colsurfb.2012.08.016.

[40] Y. Wang, D. Gao, Y. Chen, G. Hu, H. Liu, Y. Jiang, Development of N, S-doped carbon dots as a novel matrix for the analysis of small molecules by negative ion MALDI-TOF MS, RSC Adv. 6 (82) (2016) 79043–79049, https://doi.org/10.1039/C6RA12131D.

[41] M. Louleb, L. Latrous, A. Rios, M. Zougagh, E. Rodriguez-Castellon, M. Algarra, J. Soto. Detection of Dopamine in Human Fluids Using N-Doped Carbon Dots. ACS Appl. Nano Mater. 3 (2020) 8004-8011. https://doi.org/ 10.1021/acsanm.0c01461.

[42] M. Algarra, V. Moreno, J.M. Lázaro-Martínez, E. Rodríguez-Castellón, J. Soto, J. Morales, A. Benítez, Insights into the formation of N doped 3D-graphene quantum dots. Spectroscopic and computational approach, J. Coll. Interf. Sci. 561 (2020) 678–686, https://doi.org/10.1016/j.jcis.2019.11.044.

[43] K. Serec, S. Dolanski Babić, R. Podgornik, S. Tomić, Effect of Mg ions on the structure of DNA thin films: An infrared spectroscopic study, Nucleic Acid Research 44 (2016) 8456–8464, https://doi.org/10.1093/nar/gkw696.

[44] T.L. Teng-Hern, C. Kok-Gan, P. Priyia, L. Wai-Leng, C. Lay-Hong, K.T. Mehmood, L. Learn-Han, G. Bey-Hing, Targeting Membrane Lipid a Potential Cancer Cure?, Front Pharmacol. 8 (2017) 12, https://doi.org/10.3389/fphar.2017.00012.

[45] M. Kreuzer S. Stamnekovic, S. Chen P. Andjus, T. Dučić T. Lipids status and copper in a single rat astrocyte model for amyotrophic lateral sclerosis: correlative synchrotron-based X-ray and infrared imaging. J. Biophotonics 13 (2020) 202000069. https://doi.org/10.1002/jbio.202000069.

[46] D.R. Baer, M.H. Engelhard, XPS analysis of nanostructured materials and biological surface, J. Electron Spectrosc. Related Phenom. 178–179 (2010) 415–432, https://doi.org/10.1016/j.elspec.2009.09.003.

[47] J. F Moulder, W.F. Stickle, P.E. Sobol, K.D. Bomben. In: Handbook of X Ray Photoelectron Spectroscopy: A reference book of standard spectra for identification and interpretation of XPS Data, Physical Electronics, Eden Prairie, Minn., 1995.

[48] K. Ajima, T. Murakami, Y. Mizoguchi, K. Tsuchida, T. Ichihashi, S. Iijima, M. Yudasaka, Enhancement of in vivo anticancer effects of cisplatin by incorporation inside single-wall carbon nanohorns, ACS Nano. 2 (10) (2008) 2057–2064, https://doi.org/10.1021/nn800395t.

[49] L. Zhang, J. Xia, Q. Zhao, L. Liu, Z. Zhang, Functional graphene oxide as a nanocarrier for controlled loading and targeted delivery of mixed anticancer drugs, Small. 6 (4) (2010) 537–544, https://doi.org/10.1002/smll.200901680.

[50] X. Sui, C. Luo, C. Wang, F. Zhang, J. Zhang, S. Guo, Graphene quantum dots enhance anticancer activity of cisplatin via increasing its cellular and nuclear uptake. Nanom: Nanotech, Biol. Med. 12 (7) (2016) 1997–2006, https://doi.org/10.1016/j.nano.2016.03.010.

[51] Y. Ding, K. Zhai, P. Pei, Y. Lin, Y. Ma, H. Zhu, M. Shao, X. Yang, W. Tao, Encapsulation of cisplatin in a pegylated calcium phosphate nanoparticle (CPNP) for enhanced cytotoxicity to cancerous cells, J. Coll. Interf. Sci. 493 (2017) 181–189, https://doi.org/10.1016/j.jcis.2017.01.032.